

## Direct $k$ -space imaging of Mahan cones at clean and Bi-covered Cu(111) surfaces

Aimo Winkelmann<sup>1</sup>, A Akin Ünal, Christian Tusche,  
Martin Ellguth, Cheng-Tien Chiang and Jürgen Kirschner

Max Planck Institute of Microstructure Physics, Weinberg 2, 06120 Halle,  
Germany

E-mail: [winkelm@mpi-halle.mpg.de](mailto:winkelm@mpi-halle.mpg.de)

*New Journal of Physics* **14** (2012) 083027 (16pp)

Received 2 March 2012

Published 22 August 2012

Online at <http://www.njp.org/>

doi:10.1088/1367-2630/14/8/083027

**Abstract.** Using a specifically tailored experimental approach, we revisit the exemplary effect of photoemission from quasi-free electronic states in crystals. Applying a *momentum microscope*, we measure photoelectron momentum patterns emitted into the complete half-space above the sample after excitation from a linearly polarized laser light source. By the application of a fully three-dimensional (3D) geometrical model of direct optical transitions, we explain the characteristic intensity distributions that are formed by the photoelectrons in  $k$ -space under the combination of energy conservation and crystal momentum conservation in the 3D bulk as well as at the two-dimensional (2D) surface. For bismuth surface alloys on Cu(111), the energy-resolved photoelectron momentum patterns allow us to identify specific emission processes in which bulk excited electrons are subsequently diffracted by an atomic 2D surface grating. The polarization dependence of the observed intensity features in momentum space is explained based on the different relative orientations of characteristic reciprocal space directions with respect to the electric field vector of the incident light.

<sup>1</sup> Author to whom any correspondence should be addressed.

**Contents**

<b>1. Introduction</b>	<b>2</b>
<b>2. Mahan cone formation</b>	<b>3</b>
<b>3. Experiment</b>	<b>7</b>
<b>4. Results</b>	<b>8</b>
<b>5. Discussion</b>	<b>9</b>
<b>6. Summary</b>	<b>14</b>
<b>References</b>	<b>14</b>

**1. Introduction**

Due to the mismatch in the dispersion relations for photons and electrons, photoexcitation of free electrons in vacuum is inhibited by energy and momentum conservation laws [1]. In a crystal, however, the momentum that needs to be transferred to the photoelectron can be supplied by the exchange of reciprocal lattice vectors at virtually no energy cost. This is due to the infinitesimal collective recoil energy of a large number of atoms involved in such a coherent process. The mere energy conservation in photon absorption by the electrons is thus complemented by momentum conservation restrictions that are enforced by the crystal lattice. As the momentum is related to the direction of the emitted photoelectrons, momentum conservation strongly influences the actual angle-dependent intensity distributions observed in photoemission from valence band states of crystals. Specifically, in a nearly free-electron band structure, momentum and energy conservation confine photoelectron wave vectors at a specific kinetic energy to hollow cones around reciprocal lattice vectors, the so-called Mahan cones [1–5]. Since the overall *geometry* of the possible momentum transfers from the crystal is governed by the symmetry of the discrete reciprocal lattice vectors and their combinations, even photoelectrons excited from supposedly simple nearly free-electron states in a crystal can, in principle, show rather intricate intensity distributions.

Moreover, if the electrons from the primary, bulk excited, Mahan cones are elastically scattered at a two-dimensionally periodic surface structure, this amounts to a change of the surface-parallel component of the electron wave vector by a reciprocal lattice vector of the respective surface mesh. Due to energy conservation in elastic scattering, the perpendicular momentum of the photoelectrons is also changed accordingly in such surface Umklapp processes [6–10]. As we will see, this can lead to photoemission of additional electrons that initially do not have enough perpendicular momentum to overcome the surface barrier. These bulk electrons can be allowed to leave the sample after scattering at an atomic two-dimensional (2D) surface diffraction grating. Such a grating can be provided, for instance, by a periodic adsorbate superstructure.

The purpose of this paper is to illustrate the mechanism of the Mahan cone formation and the subsequent diffraction by a surface lattice for particularly transparent model systems that were investigated using a newly developed *momentum microscope*. This unique instrument allows one to map directly the intensity of photoelectrons in dependence of their  $(k_x, k_y)$ -vectors for the whole emission half-space above the sample [11, 12]. In this way, the relationships of optical transitions in reciprocal space can be most directly imaged experimentally. Understanding these basic  $k$ -dependent effects is important for the

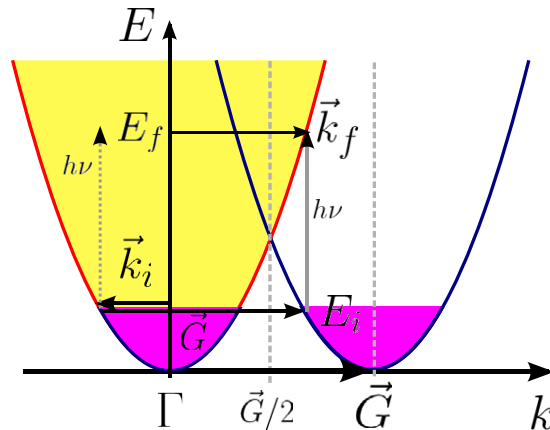


**Figure 1.** Direct optical transition in a 1D model band structure. Excitation with photon energy  $h\nu$  of an initial state at  $E_i(\vec{k}_i)$  to a final state at  $E_f(\vec{k}_f)$  via the addition of a reciprocal lattice vector  $\vec{G}$ .

interpretation of more general photoelectron momentum distribution measurements, which include, e.g., photoemission Fermi surface mapping of three-dimensional (3D) [13–17] and lower dimensional systems [18–21], as well as for investigations of the orbital composition of valence bands using polarized light [22–25].

The system we investigated is the Cu(111) surface, which shows a well-known direct optical transition between nearly free-electron sp-bands for photon energies near 6 eV. When Bi is deposited on Cu(111), it forms a  $(\sqrt{3} \times \sqrt{3})R30^\circ$  superstructure which can act as an atomic diffraction grating for photoelectrons excited in the bulk and transmitted through the surface. This leads to the very peculiar photoelectron momentum distributions we observe. As an important new aspect of our work, we show how the application of polarized light can provide useful information on the specific crystallographic conditions of Mahan cone backfolding on Bi/Cu(111).

## 2. Mahan cone formation

In this section, we recall the mechanism of Mahan cone formation with an emphasis on the 3D character of this process in a bulk system.

In order to understand the geometrical relationships in three  $k$ -space dimensions, it is instructive to start with the well-known  $E(k)$  dispersion for a free electron in one dimension, shown in figure 1. For a free electron, the dispersion is  $E(k) = \frac{\hbar^2}{2m}k^2$ . The dashed gray arrow in figure 1 indicates the energy increase due to absorption of a photon. This process will increase the initial energy  $E_i$  of the electron by  $h\nu$  but leave the momentum nearly constant at  $\vec{k}_i$  due to the vanishingly low momentum of the photon itself. Without a change in momentum, however, the electron cannot fulfill energy and momentum conservation simultaneously, as is seen from the absence of an electronic state at  $\vec{k}_i$  at the final state energy  $E_f$ . In the presence of a periodic real-space potential, the electronic band structure repeats itself in  $k$ -space with the period of a reciprocal lattice vector. If this periodic potential is assumed to be very weak, the crystal band structure is approximated simply by copies of the free-electron parabola shifted by reciprocal lattice vectors (‘empty lattice approximation’ [26]), neglecting, e.g., the formation of

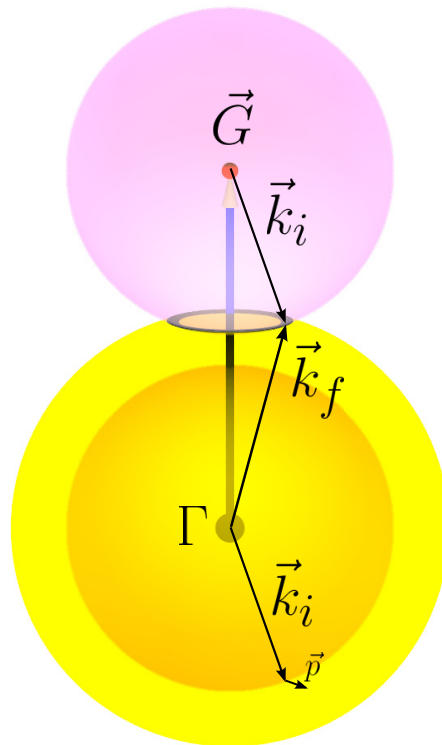


**Figure 2.** Photoemission from quasi-free-electron states: iso-energy surfaces of final states  $\vec{k}_f$  (yellow) and initial states  $\vec{k}_i$  (blue) are spheres around  $\Gamma$  with radius  $|\vec{k}_{i,f}| = \sqrt{\frac{2m_{\text{eff}}}{\hbar^2} E_{i,f}}$  as determined by a quasi-free-electron dispersion relation. Energy transfer  $h\nu$  from the incident radiation to the detected photoelectron at  $E_f$  requires  $E_f = E_i + h\nu$ , which results in the different diameters of the electron spheres. Because the *photon* momentum is only very small  $|\vec{p}| \ll |\vec{k}_{i,f}|$ , momentum conservation for the free electron cannot be attained simultaneously:  $\vec{k}_i + \vec{p} \neq \vec{k}_f$ , i.e., the photon cannot connect the two  $k$ -spheres centered at  $\Gamma$  in momentum space. In the empty lattice free-electron band structure  $E = \frac{\hbar^2}{2m} (\vec{k} - \vec{G})^2$ , the translation of the initial state iso-energy-surface centered at  $\Gamma$  by a reciprocal lattice vector  $\vec{G}$  allows simultaneous energy and momentum conservation (even with vanishing photon momentum  $\vec{p}$ ). An optical transition is possible for  $\vec{k}_f$ -vectors on the intersection of the translated initial state sphere centered at  $\Gamma + \vec{G}$  with the final state sphere centered at  $\Gamma$ , with  $\vec{k}_f = \vec{k}_i + \vec{G}$ . The geometrical shape of the intersection of these two spheres is a ring of final state  $\vec{k}_f$ -vectors around the direction of  $\vec{G}$ , forming the final state *Mahan cone*.

band gaps at the Brillouin zone boundary  $\vec{G}/2$ . Photoemission in the periodic band structure is then possible by the addition of a reciprocal lattice vector  $\vec{G}$  to the initial state so that  $\vec{k}_f = \vec{k}_i + \vec{G}$  and  $E_f = E_i + h\nu$  [1].

We can now adapt the results of the one-dimensional (1D) model sketched in figure 1 to three  $k$ -space dimensions. As shown in figure 2, in a quasi-free-electron model the  $\mathbf{k}$ -vectors

of the photoemitted electrons are determined by a final state free-electron spherical isosurface (yellow), the diameter of which is determined by the kinetic energy of the photoelectron in the crystal from  $E = \frac{\hbar^2}{2m} |\vec{k}|^2$  as  $|\mathbf{k}| = 0.512 \text{ \AA}^{-1} \sqrt{E/eV}$ . Geometrically, this means that the electron energy depends on the magnitude of the momentum, but not on the direction, and this directly implies spherical energy isosurfaces in the 3D  $\mathbf{k}$ -space. The  $k$ -space isospheres of figure 2 can be directly related to the more familiar  $E(k)$ -plots, where the free-electron energy is drawn as a parabola as a function of  $|k|$  as seen in figure 1. Using the free-electron parabola, we can determine the isosphere radius from the value of  $|k|$  at a given energy.

The energy transfer  $h\nu$  from the incident radiation to the detected photoelectron at  $E_f$  requires that the initial state energy is  $E_i = E_f - h\nu$ , which consequently leads to a smaller diameter of the initial state isosurface. It is important to note that energy conservation by itself does not restrict the possible  $\mathbf{k}$ -vectors of the photoemitted electrons apart from being located somewhere on the final state isosphere.

However, in addition to energy conservation, momentum conservation must also be considered. Generally speaking, the momentum *vector* which is delivered by the interaction process must connect specific states on the initial and final state isospheres for both energy *and* momentum conservation laws to be fulfilled together in the excitation process. If this is possible at all, these specific combinations of initial and final state  $\mathbf{k}$ -vectors will be selected in the excitation process, resulting finally in the  $\mathbf{k}$ -dependence of the excited photoelectron intensity. Because the *photon* momentum in the ultraviolet (UV) and vacuum UV regions is only very small  $|\vec{p}| \ll |\vec{k}_{i,f}|$ , we see that momentum conservation for the free electron can actually not be attained simultaneously:  $\vec{k}_i + \vec{p} \neq \vec{k}_f$ , i.e., the photon momentum vector cannot connect in any way the two  $k$ -spheres centered at  $\Gamma$ . The initial state electron cannot make a transition from a state on one isosphere to a state on the other one because the photon simply does not supply the necessary momentum together with its energy quantum. However, in the empty lattice free-electron band structure  $E = \frac{\hbar^2}{2m} (\vec{k} - \vec{G})^2$ , the translation of the initial state iso-energy surface centered at  $\Gamma$  by a reciprocal lattice vector  $\vec{G}$  leads to simultaneous energy and momentum conservation at the intersection of the translated initial state sphere centered at  $\Gamma + \vec{G}$  with the final state sphere centered at  $\Gamma$ , where  $\vec{k}_f = \vec{k}_i + \vec{G}$ . Physically, the crystal provides the momentum change  $\hbar\vec{G}$  of the electron by recoiling with the discrete momentum  $-\hbar\vec{G}$ , which is connected only with an infinitesimal recoil energy of  $(\hbar^2\vec{G}^2)/2M_{\text{crystal}}$ . Thus, in the direct optical transition, the photon supplies the energy and the crystal the momentum.

As we see in figure 2, the intersection of the crystal-momentum-translated initial state sphere with the final state sphere results in allowed  $\mathbf{k}$ -vectors on a circular contour, where both energy and momentum conservation are fulfilled. Viewed as emission directions, the  $\mathbf{k}$ -vectors of the electrons making up the intersection circle form a hollow cone, the Mahan cone [1, 5].

Since there are specific reciprocal lattice vectors involved in a direct optical transition, the symmetry of the crystal should be reflected in the  $\mathbf{k}$ -dependent photoelectron intensity. In an fcc crystal, for reciprocal lattice vectors directed close to the equivalent  $\langle 111 \rangle$  directions, we see in figure 3 that we should observe ring-like internal distributions of photoelectrons around the symmetry-related  $\Lambda$ -directions for excitation between nearly free electron-like bands. Such a situation is given for the surfaces of Cu(111) and Ag(111) for photon energies near 6 eV, where electrons are excited from occupied to unoccupied nearly free sp-bands [27–29]. The fact that these states are only approximately free-electron-like is seen from the fact that the experimental

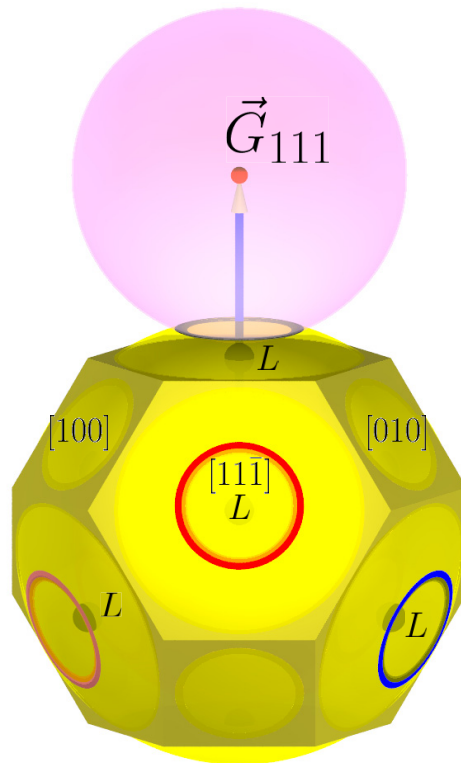


**Figure 3.** Direct optical transition involving the reciprocal lattice vector  $\mathbf{G}_{111}$ , pointing along the normal direction of an fcc(111) surface. According to the symmetry of the Brillouin zone in the fcc lattice, similar optical *bulk* transitions (seen as differently colored circles) are also induced near equivalent L points. These additional transitions involve reciprocal lattice vectors that are related to  $\mathbf{G}_{111}$  by the respective symmetry operation of the fcc crystal structure. We show the approximate situation for photon energies near 6 eV in Cu and Ag.

distributions are not perfectly circular but show a threefold symmetry as expected for the  $\langle 111 \rangle$  zone axes in an fcc crystal (see below). From the Mahan cones shown in figure 3, only the elastic electrons moving near to the [111] surface normal can actually leave the sample on the top side for the photon energies applied in our experiment. The photoelectrons from the vicinity of the other symmetry equivalent  $\Lambda$ -directions, which are also seen in figure 3, would be internally back-reflected at the surface barrier or correspond to emission at the bottom of the sample (this is the case for the  $[\bar{1}\bar{1}\bar{1}]$  cone at the bottom hexagonal face of the Brillouin zone polyhedron, not visible in figure 3).

Figures 2 and 3 have been produced using a 3D ray-tracing program [30], which allows us to change the viewpoint and projection plane easily. While keeping the intuitive insight into the full 3D origin of bulk Mahan formation, this reduces the problem of finding the surface-projected  $\mathbf{k}$ -vectors of the respective bulk transitions to a simple change of the viewpoint in an orthographic projection. In our analysis of (111) surfaces below, we will thus be concerned with views of figure 3 from a viewpoint that lies along the surface normal direction.

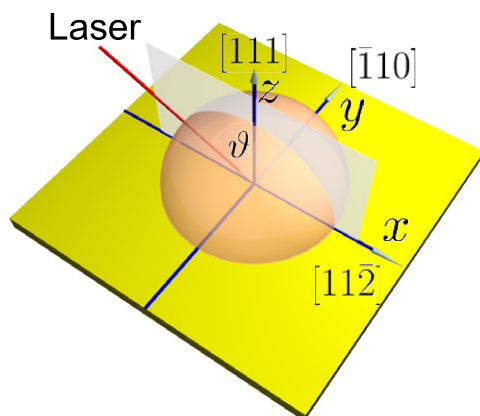


**Figure 4.** The experimental coordinate system. The 6 eV laser radiation is incident along the angle  $\vartheta = 65^\circ$  in the  $x$ - $z$  plane. The electron-optical axis of the momentum microscope is along the  $[111]$   $z$ -direction. The  $x$ -axis is along the  $[11\bar{2}]$  direction and the  $y$ -axis is along the  $[\bar{1}10]$  direction of the bulk fcc crystals. The s-polarized incident light has its  $E$ -field polarization vector along the  $y$ -direction, and the p-polarized light is in the  $x$ - $z$ -plane.

### 3. Experiment

The momentum microscope we used in this investigation is a combination of a photoelectron emission microscope column with an aberration-corrected electrostatic electron energy analyzer [11]. The instrument is unique in the sense that it can record the energy-resolved photoemission intensity in the whole emission hemisphere above the sample surface simultaneously in a single run, including an optional spin-polarization analysis [31]. For comparison, a conventional angle-resolved photoemission setup with a two-dimensional (2D) detector measures energy-dependent momentum distributions only in a single azimuth (with a limited acceptance opening angle), so that the sample has to be rotated to sequentially acquire complete 2D  $k$ -space data.

The experimental coordinate system is shown in figure 4. In this study, we used linearly polarized light from an ultrafast Ti:Sa laser, with the p-polarized light having the  $E$ -field polarization vector in the  $x$ - $z$ -plane and the s-polarized light with the  $E$ -field vector along the  $y$ -direction. The excitation light of 6 eV was produced by twofold nonlinear optical second harmonic generation from the 1.5 eV laser fundamental using  $\beta$ -BaB<sub>2</sub>O<sub>4</sub> (BBO) crystals. For comparison, we also measured two-photon photoemission using a single-photon energy of 3.1 eV in the same experiment. The radiation is incident from a viewport in the  $x$ - $z$  plane for  $\vartheta = 65^\circ$ . The electron-optical axis of the momentum microscope is along the  $z$ -direction. The energy resolution was  $< 200$  meV.

Clean surfaces of Cu(111) were prepared by standard procedures. Bi was deposited at 400 K sample temperature from an evaporation source by electron beam heating. The formation of the  $(\sqrt{3} \times \sqrt{3})R30^\circ$  Bi superstructure [32] was checked by medium energy electron diffraction during deposition. During the measurements, the samples were kept at 170 K by liquid nitrogen cooling.

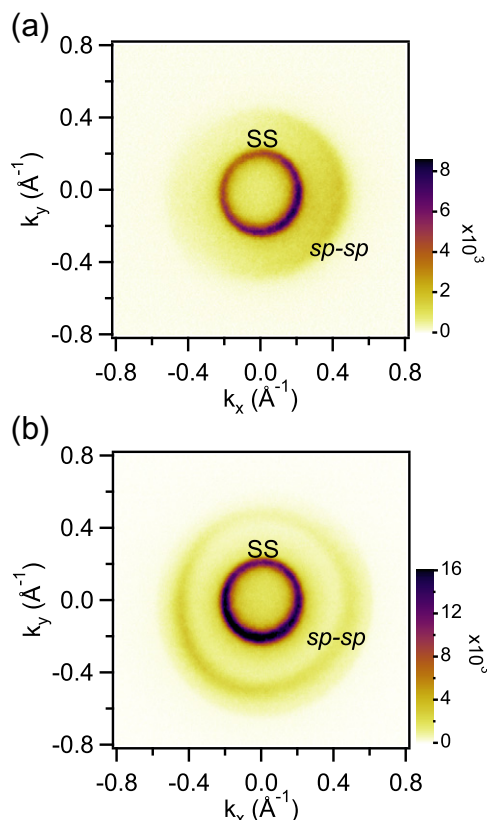


**Figure 5.** Photoemission from clean Cu(111) with p-polarized light in 1PPE and 2PPE for an initial state energy of  $E_F - 50$  meV (for the setup see figure 4). Photoemission is confined to a circular region in the  $k_{\parallel}$ -plane, limited by the maximum surface-parallel momentum allowed by the kinetic energy measured (‘photoemission horizon’). The 2PPE pattern shows the sp–sp Mahan cone emission ring clearly inside the photoemission horizon due to the slightly higher total transition energy of 6.2 eV as compared to 6 eV in 1PPE. The central ring in both patterns at SS is the Shockley surface state. (a) Cu(111), 1PPE,  $h\nu = 6$  eV; and (b) Cu(111), 2PPE,  $2h\nu = 6.2$  eV.

#### 4. Results

In figure 5, we show the measurements from the clean Cu(111) sample. These measurements were carried out in one-photon photoemission (1PPE) and two-photon photoemission (2PPE). The 2PPE experiment allowed us to employ a slightly higher total transition energy of  $2h\nu = 6.2$  eV compared to the single photon energy of  $h\nu = 6.0$  eV in 1PPE (this is due to the second harmonic generation limits of BBO). Panels (a) and (b) of figure 5 show the  $k_x$ ,  $k_y$ -measurements from initial states at 50 meV below the Fermi level. The 2PPE pattern has a slightly larger diameter due to the higher kinetic energy and thus a higher maximum surface-parallel momentum of the photoelectrons. In the center of both images, we see the Fermi contour of the Shockley surface state (SS). Both the binding energy and the Fermi vector of the Shockley state we observed [33] are consistent with well-known literature values [34]. Of central interest for this paper, however, are not the Shockley state features, but the ring-like intensity toward the outer rim of the observed pattern, which is marked by ‘sp–sp’ in figure 5. We see a clear ring for

Cu(111) in 2PPE, while in 1PPE there is only an intensity increase in the vicinity of the edge of the experimentally accessible reciprocal space region. This ring-like intensity can be assigned to direct optical transitions between nearly free-electron sp-bands, which are well known to occur at Cu(111) and Ag(111) surfaces [27–29]. These direct optical transitions between sp bands form a [111] Mahan cone, according to the introductory discussion and as shown in figure 3, because their 3D  $E(\vec{k})$  dispersion can be well approximated by a quasi-free behavior. For quasi-free electrons in the empty lattice approximation [26] (resulting in the crystal-momentum-translated spherical isosurfaces discussed above), we should see a circular Mahan cone ring. A closer inspection of the 2PPE measurement in figure 5(b), however, shows the actual threefold distorted character of the Mahan cone emission, which has also been seen previously [29] using serial 2PPE measurements with sample rotation. The threefold distortion is expected as the relevant sp states are influenced by the crystal potential near the zone boundary and the bulk crystal shows threefold symmetry around the  $\langle 111 \rangle$  zone axes. This was also corroborated by theoretical DFT calculations of the relevant Fermi surface region [29]. As we will see below, after deposition of Bi, the [111] Mahan cone also becomes completely visible in 1PPE due a reduction of the work function. Then we can also see the threefold distortion of the sp–sp Mahan cone in 1PPE in figure 6(b). As our main emphasis in this paper is a discussion of the Mahan cone mechanism in the initial to final state transition, we will not discuss here the 2PPE measurements from Bi/Cu(111), which include additional intermediate state effects [35].

We now turn to the changes in the photoemission momentum patterns resulting from the formation of a  $(\sqrt{3} \times \sqrt{3})R30^\circ$  bismuth surface alloy on Cu(111). By a reduction of the work function via deposition of bismuth, the kinetic energy and thus the maximum momentum of the Fermi level photoelectrons are increased, enlarging the photoemitted region in  $k$ -space. The resulting 1PPE patterns are shown in figures 6(b) and (c) for p- and s-polarized incident light, respectively. Compared to the clean Cu(111) pattern in panel (a), the photoemission  $k$ -space region is extended corresponding to a work function reduction by 0.5 eV in panels (b) and (c) of the figure. In the patterns from Bi-covered surfaces, the Shockley surface state feature ‘SS’ of clean Cu(111) is absent, indicating the suppression of this state after Bi deposition. Instead, the pattern in the central region shows two concentric circles (marked by the ‘R’ in figure 6) surrounded by a hexagonal feature (marked by the ‘h’). These features correspond to electronic states of the Bi surface alloy, which are known to exhibit important spin–orbit coupling effects [35, 36] but which will not be discussed in the present paper.

Instead, we draw attention to the outer ring-like intensity surrounding the hexagonal feature ‘h’, which obviously corresponds to the sp–sp transition Mahan cone ring that is now completely unveiled by the work function reduction. Moreover, we see additional contributions (marked by ‘CF’ in figure 6), which seem to be attached to the central primary Mahan cone ring and which look like ‘chicken-feet’. These additional contributions are strongly polarization dependent, as we can see from the characteristic, complementary patterns for p-polarized light (figure 6(b)) and for the s-polarized light (figure 6(c)). When the patterns for both polarizations are added, we obtain nearly threefold symmetric contributions around the primary Mahan cone, as can be seen in figure 7. We note that for Bi/Ag(111) we made very similar observations.

## 5. Discussion

In order to explain the features observed in the experiment, we visualize the relevant optical transitions and scattering processes in  $k$ -space. The surface-parallel extension of the Mahan

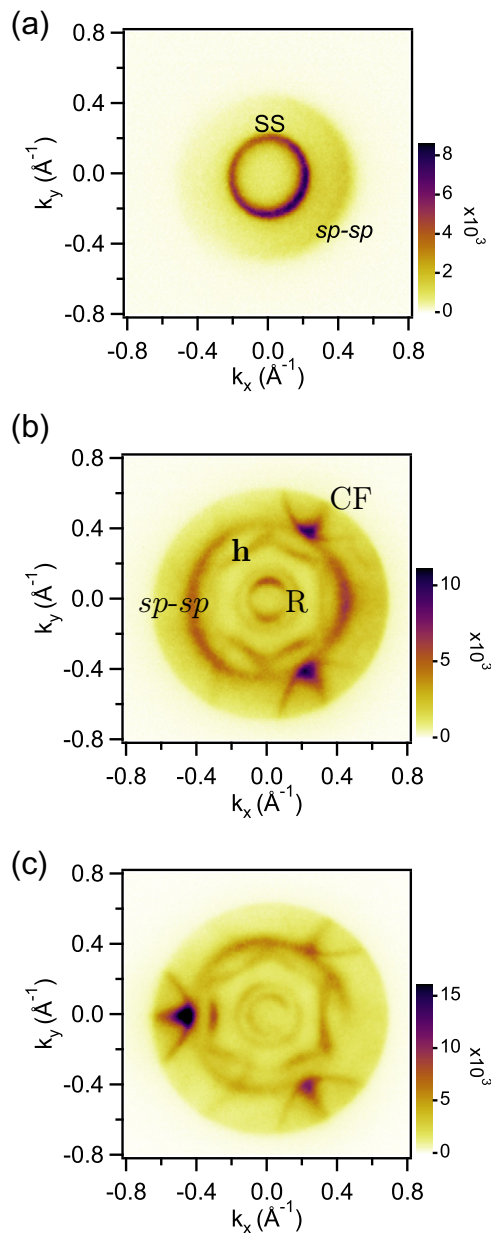


**Figure 6.** Photoemission from  $(\sqrt{3} \times \sqrt{3})R30^\circ$  Bi/Cu(111),  $h\nu = 6$  eV, initial state level at  $E_F - 50$  meV (middle and lower panels) compared to clean Cu(111) in the top panel. The concentric rings at ‘R’ and the hexagonal feature ‘h’ belong to the well-known Rashba-split states of the Bi surface alloy. The bulk Mahan cone ring is marked by ‘sp-sp’. Additional ‘chicken-feet’-like structures are seen at ‘CF’ and at threefold rotationally equivalent positions in the p-polarized (b) and the s-polarized (c) patterns.

cone sp–sp emission can be directly obtained by redrawing the 3D objects of figure 3 in an orthographic projection along the [111]-axis, so that the  $k_{\parallel}$ -components of the (111) surface are in the paper plane. This projection into the sample surface plane is rather trivially achieved by selecting an appropriate viewpoint and an orthographic projection in the 3D ray-tracing

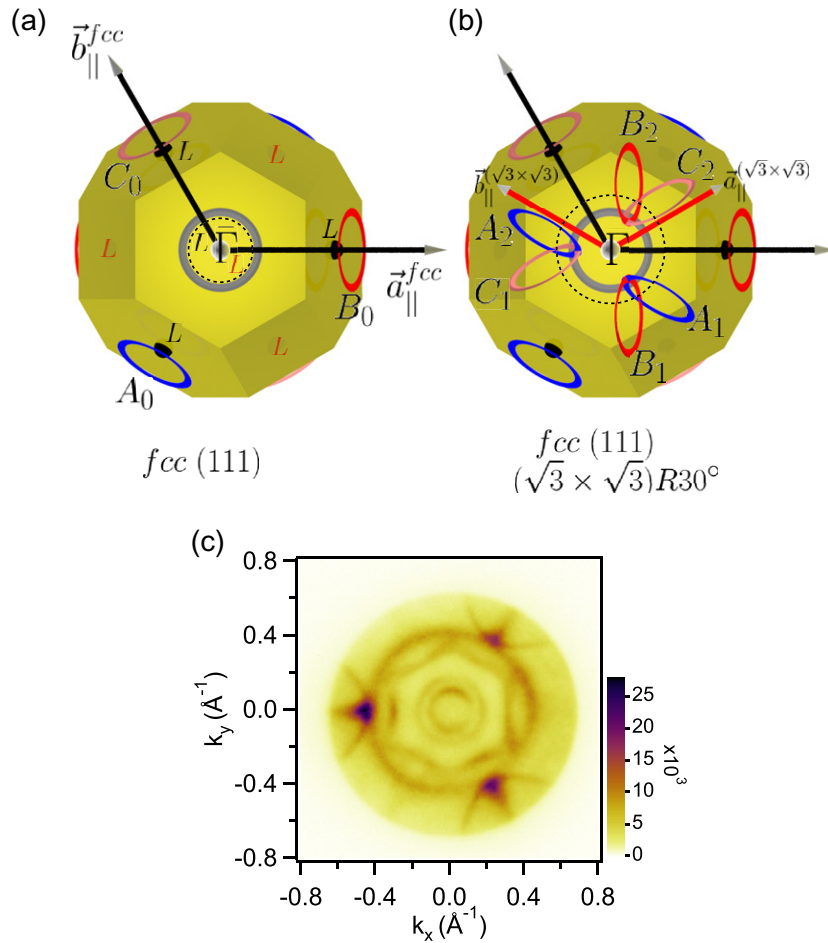


**Figure 7.** (a) Projection of figure 3 along the [111] direction, corresponding to an fcc(111) surface in the paper plane with the fcc surface reciprocal lattice vectors  $\vec{a}_{||}^{\text{fcc}}$  and  $\vec{b}_{||}^{\text{fcc}}$ . For the bulk, there are four equivalent direct optical transitions near equivalent L points (i.e., the central Mahan cone ring plus  $A_0, B_0, C_0$ ), which excite photoelectrons moving with components parallel to the [111] front direction of the sample and four other transitions toward the  $[\bar{1}\bar{1}\bar{1}]$  back direction. (b) In the presence of a  $(\sqrt{3} \times \sqrt{3})R30^\circ$  surface lattice, the bulk transitions can be translated in the surface plane by the respective surface reciprocal lattice vectors  $\vec{a}_{||}^{(\sqrt{3} \times \sqrt{3})}$  and  $\vec{b}_{||}^{(\sqrt{3} \times \sqrt{3})}$ . Colors indicate the respective bulk transition from which the translated copies are derived. (c) Experimental pattern from Bi/Cu(111); the average of s and p polarizations shown in figure 6. The Mahan cone structures visible in the measured data can be compared with the region of the observed  $k_{||}$ -space indicated as a black dashed circle in (b).

simulation, with the advantage that the 3D character of the bulk  $\mathbf{k}$ -space is fully retained. The result of this operation for the clean fcc surfaces is shown in figure 7(a), where we also show the fcc(111) surface reciprocal lattice vectors  $\vec{a}_{||}^{\text{fcc}}$  and  $\vec{b}_{||}^{\text{fcc}}$ . Again, we point to the intrinsically 3D character of the objects shown in figure 7. There, we see the central Mahan cone ring projected around  $\bar{\Gamma}$ . The projections of the two L points along [111] and  $[\bar{1}\bar{1}\bar{1}]$  coincide with  $\bar{\Gamma}$ , while

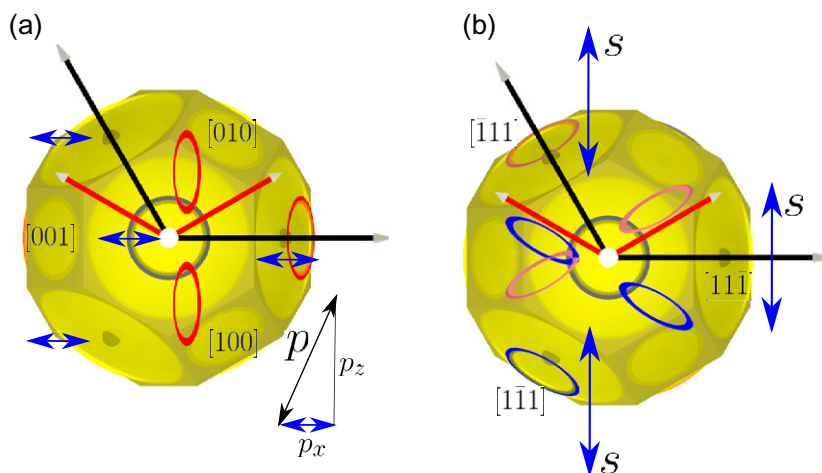


**Figure 8.** Polarization-dependent excitation of primary bulk Mahan cones and backfolding by  $(\sqrt{3} \times \sqrt{3})R30^\circ$  Bi/Cu(111); the optical plane is along  $k_y = 0$ . Indicated is the major bulk direction perpendicular to the faces of the bulk Brillouin zone polyhedron. Please compare with the experimental data in figures 6(b) and (c). (a) p-polarized light with large component along the  $[111]$  Mahan cone (red) and (b) s-polarized light with large component along the  $[\bar{1}\bar{1}\bar{1}]$  and  $[1\bar{1}\bar{1}]$  Mahan cones (blue and brown).

transitions near three other L points lead to photoelectrons moving upwards to the top surface of the crystal ( $A_0, B_0, C_0$  in figure 7(a)), while three other L point transition cones (largely hidden by the Brillouin zone polyhedron) have wave vectors pointing toward the lower surface of the crystal (compare also with figure 8 for the major bulk crystallographic directions). As we can see from figure 7(a), the electron wave vectors relevant to the Mahan cones  $A_0, B_0, C_0$  have components parallel to  $[111]$  and thus point out of the surface (paper) plane. Due to the 2D projection of the three outward pointing Mahan cones  $A_0, B_0, C_0$ , these appear as ellipses, while in three dimensions they, of course, remain circular around the respective *bulk* directions. Because the surface-parallel  $k_{\parallel}$  components of the three symmetry-related cones are well outside the photoemission horizon of the clean surfaces, the respective photoelectrons cannot leave the crystal although their total energy is higher than the work function. The *perpendicular* momentum of these electrons is insufficient to overcome the surface barrier. The photoemission horizons for the (111) surfaces are shown schematically in figure 7 as the dashed black circles (where for the clean surface in figure 7(a), the sp–sp transition is slightly outside the photoemission horizon of the experimental 1PPE measurements in figure 6(a)).

When the clean fcc surface is covered by the Bi alloy, the  $(\sqrt{3} \times \sqrt{3})R30^\circ$  structure leads to additional reciprocal lattice vectors  $\vec{a}_{\parallel}^{(\sqrt{3} \times \sqrt{3})}$  and  $\vec{b}_{\parallel}^{(\sqrt{3} \times \sqrt{3})}$ , which, compared to the clean surface vectors, are shortened by a factor of  $1/\sqrt{3}$  and rotated by  $30^\circ$ , as can be seen in the right part of figure 7 by the red arrows. In the surface plane, diffraction by the surface grating corresponds to parallel translations of the primary bulk Mahan cones  $A_0, B_0, C_0$  along combinations of surface reciprocal lattice vectors. The result is seen in the right part of figure 7 by the shifted copies of the bulk Mahan cones, which are labeled and colored according to the primary cone from which they originate ( $A_0 \rightarrow A_1, A_2$ ;  $B_0 \rightarrow B_1, B_2$ ; and  $C_0 \rightarrow C_1, C_2$ ). The

**Table 1.** Direction cosines of crystal-symmetry equivalent primary Mahan cone directions relative to the polarization unit vectors of the incident light.

$\vec{G}_{hkl}$	$\vec{p}$	$\vec{s}$
	$1/1.44[1\ 1\ 0.256]$	$1/\sqrt{2}[\bar{1}\ 1\ 0]$
$1/\sqrt{3}[111]$	0.91	0.00
$1/\sqrt{3}[11\bar{1}]$	0.70	0.00
$1/\sqrt{3}[1\bar{1}1]$	0.10	-0.82
$1/\sqrt{3}[\bar{1}11]$	0.10	+0.82

scattering processes lead to the formation of a combination of the initial primary Mahan cone around [111] with in each case two shifted ellipses that form the ‘chicken feet’-like structure observed in experiment. As seen from figure 7(b), very good agreement is reached for the position and the shape of the primary and secondary Mahan cone features compared to the polarization-averaged experimental measurement shown in figure 7(c). The mechanism we have explained here should be completely similar for Cu(111) and Ag(111), with the quantitative differences determined by the different work functions and the positions of the upper and lower sp bands with respect to the Fermi level.

The purely geometrical relationships of the observed structures are thus very nicely explained by the 3D geometrical model of energy isosurfaces in  $k$ -space that we have introduced above. It remains to clarify the sensitivity of the Bi/Cu(111) Mahan cone structures to the polarization of the incident light as is seen in the experimental data taken with p- and with s-polarized light in figures 6(b) and (c), respectively. The key to understanding these patterns lies in the normal emission Mahan cone around the [111] direction, which we observe to be excited much more efficiently with p-polarized light as compared with s-polarized light. The different polarization sensitivity is seen from a comparison of the experimental data in figures 6(b) and (c), where in panel (c) we observe an intensity reduction of one order of magnitude of the primary sp–sp Mahan cone for s-polarized light. This can be explained by a dominating  $p_z$ -like orbital character of the relevant Cu initial states on the (111) surface [37].

In effect, the optical transitions leading to the Mahan cone formation are most sensitive to the polarization component of the light, which is approximately parallel to the [111] direction, and, by symmetry, this should apply also to the transitions near the other three equivalent directions:  $[\bar{1}11]$  ( $C_0$ ),  $[1\bar{1}1]$  ( $A_0$ ) and  $[11\bar{1}]$  ( $B_0$ ) (see figures 7 and 8(b)). However, for the two possible incident polarizations, the projections of the electric field components along these crystal-symmetry equivalent directions are characteristically different for p- and for s-polarized light, as we can see from the direction cosines of the polarization vectors of the incident light relative to the four crystal-symmetry equivalent bulk Mahan cone directions in table 1. With reference to table 1, we can also graphically see in figure 8(a) that the incident p-polarized light has a large projected component on the [111] and  $[1\bar{1}1]$  directions (0.91 and 0.70, respectively), while it has a much smaller component of 0.10 along the two other directions ( $[\bar{1}11]$  and  $[11\bar{1}]$ ). As shown in figure 8(a), the p-polarized light has its major component out of the drawing plane in the surface normal  $z$ -direction and a small  $x$ -component. The values of the  $z$  and  $x$  components are determined by the incidence angle of  $65^\circ$  shown in figure 4. The photoemitted intensity is proportional to the square of the electric field, which leads to an effective suppression of the  $[\bar{1}11]$  and  $[11\bar{1}]$  Mahan cones under  $p$  excitation. Instead, we have a dominant excitation

of the  $[111]$  and  $[11\bar{1}]$  Mahan cones and a corresponding backfolding from the  $[11\bar{1}]$  direction that results in the two features away from the optical plane seen in the experimental data in figure 6(b). In contrast, the  $s$ -polarized light has large components of 0.82 on the  $[\bar{1}11]$  and  $[1\bar{1}1]$  directions and thus excites the respective Mahan cones, while the  $[11\bar{1}]$  Mahan cone is suppressed because the  $s$ -polarization is orthogonal to  $[11\bar{1}]$  (table 1). The backfolding from the two  $s$ -excited Mahan cones then leads to the features on the optical plane and above and below this plane (figure 6(c)), complementary to the  $p$ -excited features.

Thus, our considerations starting from the polarization dependence of the primary  $[111]$  Mahan cone allowed us to consistently interpret the polarization effects in the full intensity pattern including the surface-diffracted Mahan cones. The analysis via direction cosines is simplified but shows the correct trends; a more quantitative treatment would also need to consider the optical properties of the crystal, where the refractive index leads to a modified electric field vector inside the sample.

## 6. Summary

In our  $k$ -space photoemission observations applying the momentum microscope, photoelectrons excited from supposedly simple quasi-free-electron states in a crystal provide rather intricate  $(k_x, k_y)$ -intensity distributions. This is analogous and complementary to the effects of crystal symmetry in the simplest empty-lattice free-electron states, which are known to result nevertheless in quite involved  $(E, k)$ -dependent electron band structure plots (see, e.g., [26, p 161]).

We have illustrated the mechanism of Mahan cone photoemission and backfolding by a surface lattice. To achieve this, we measured clean fcc Cu(111) surfaces in comparison to a  $(\sqrt{3} \times \sqrt{3})R30^\circ$  Bi surface alloy. We applied a simple free-electron description with direct optical transitions between spherical energy isosurfaces in 3D  $k$ -space and their respective projections into the subspace of surface-parallel momenta. The characteristic polarization dependence of the optical transitions in crystal-symmetry equivalent bulk directions was explained by the symmetry breaking that is induced by the fixed orientation of the respective polarization vector of the incident light relative to the crystal structure.

## References

- [1] Hüfner S 2003 *Photoelectron Spectroscopy* 3rd edn (Berlin: Springer) ISBN 978-3540418023
- [2] Mahan G 1970 Theory of photoemission in simple metals *Phys. Rev. B* **2** 4334–50
- [3] Smith N and Spicer W 1969 Photoemission studies of the alkali metals I. Sodium and potassium *Phys. Rev.* **188** 593–605
- [4] Fan H 1945 Theory of Photoelectric emission from metals *Phys. Rev.* **68** 43–52
- [5] Margaritondo G and Weaver J H 1985 Photoemission spectroscopy of valence states *Methods of Experimental Physics, Solid State Physics: Surfaces* vol 22, ed R L Park and M G Lagally (London: Academic) pp 127–85
- [6] Kane E 1964 Implications of crystal momentum conservation in photoelectric emission for band-structure measurements *Phys. Rev. Lett.* **12** 97–8
- [7] Anderson J and Lapeyre G 1976 Chemisorption-induced surface umklapp processes in angle-resolved synchrotron photoemission from  $W(001)$  *Phys. Rev. Lett.* **36** 376–9
- [8] Westphal D and Goldmann A 1983 Adsorbate-induced umklapp processes in photoemission from Cl on Cu *Surf. Sci.* **126** 253–7

- [9] Paolucci G 1984 Photoemission band mapping via surface umklapp *Solid State Commun.* **52** 937–40
- [10] Rader O and Shikin A 2004 An elastic ‘sieve’ to probe momentum space: Gd chains on W(110) *Phys. Rev. Lett.* **93** 256802
- [11] Krömker B, Escher M, Funnemann D, Hartung D, Engelhard H and Kirschner J 2008 Development of a momentum microscope for time resolved band structure imaging *Rev. Sci. Instrum.* **79** 053702
- [12] Winkelmann A, Tusche C, Ünal A A, Ellguth M, Henk J and Kirschner J 2012 Analysis of the electronic structure of copper via two-dimensional photoelectron momentum distribution patterns *New J. Phys.* **14** 043009
- [13] Gaylord R, Jeong K and Kevan S 1989 Experimental Fermi surfaces of clean and hydrogen-covered W(110) *Phys. Rev. Lett.* **62** 2036–9
- [14] Santoni A, Terminello L J, Himpsel F J and Takahashi T 1991 Mapping the fermi surface of graphite with a display-type photoelectron spectrometer *Appl. Phys. A* **52** 299–301
- [15] Aebi P, Osterwalder J, Fasel R, Naumovic D and Schlapbach L 1994 Fermi surface mapping with photoelectrons at UV energies *Surf. Sci.* **307–309** 917–21
- [16] Hoesch M, Greber T, Petrov V N, Muntwiler M, Hengsberger M, Auwärter W and Osterwalder J 2002 Spin-polarized Fermi surface mapping *J. Electron Spectr. Rel. Phenom.* **124** 263–79
- [17] Kotsugi M, Kuch W, Offi F, Chelaru L I and Kirschner J 2003 Microspectroscopic two-dimensional Fermi surface mapping using a photoelectron emission microscope *Rev. Sci. Instrum.* **74** 2754
- [18] Crain J, Altmann K, Bromberger C and Himpsel F 2002 Fermi surfaces of surface states on Si(111)-Ag, Au *Phys. Rev. B* **66** 205302
- [19] Crain J N, Kirakosian A, Altmann K N, Bromberger C, Erwin S C, McChesney J L, Lin J-L and Himpsel F J 2003 Fractional band filling in an atomic chain structure *Phys. Rev. Lett.* **90** 176805
- [20] Barke I, Bennewitz R, Crain J, Erwin S, Kirakosian A, McChesney J and Himpsel F 2007 Low-dimensional electron gas at semiconductor surfaces *Solid State Commun.* **142** 617–26
- [21] Gioni M, Pons S and Frantzeskakis E 2009 Recent ARPES experiments on quasi-1D bulk materials and artificial structures *J. Phys.: Condens. Matter* **21** 023201
- [22] Daimon H and Matsui F 2006 Two-dimensional angle-resolved photoelectron spectroscopy using a display analyzer: atomic orbital analysis and characterization of the valence band *Prog. Surf. Sci.* **81** 367–86
- [23] Liu Y, Bian G, Miller T and Chiang T-C 2011 Visualizing electronic chirality and berry phases in graphene systems using photoemission with circularly polarized light *Phys. Rev. Lett.* **107** 166803
- [24] Hwang C, Park C-H, Siegel D, Fedorov A, Louie S and Lanzara A 2011 Direct measurement of quantum phases in graphene via photoemission spectroscopy *Phys. Rev. B* **84** 125422
- [25] Gierz I, Henk J, Höchst H, Ast C and Kern K 2011 Illuminating the dark corridor in graphene: polarization dependence of angle-resolved photoemission spectroscopy on graphene *Phys. Rev. B* **83** 121408
- [26] Ashcroft N W and Mermin N D 1976 *Solid State Physics* (New York: Thomson Learning)
- [27] Pawlik S, Burgermeister R, Bauer M and Aeschlimann M 1998 Direct transition in the system Ag(111) studied by one- and two-photon photoemission *Surf. Sci.* **402–404** 556–60
- [28] Winkelmann A, Sametoglu V, Zhao J, Kubo A and Petek H 2007 Angle-dependent study of a direct optical transition in the sp bands of Ag(111) by one- and two-photon photoemission *Phys. Rev. B* **76** 195428
- [29] Hengsberger M, Baumberger F, Neff H, Greber T and Osterwalder J 2008 Photoemission momentum mapping and wave function analysis of surface and bulk states on flat Cu(111) and stepped Cu(443) surfaces: a two-photon photoemission study *Phys. Rev. B* **77** 085425
- [30] *Persistence of Vision Raytracer* 2004 [www.povray.org/download/](http://www.povray.org/download/)
- [31] Tusche C, Ellguth M, Ünal A A, Chiang C.-T., Winkelmann A, Krasnyuk A, Hahn M, Schönhense G and Kirschner J 2011 Spin resolved photoelectron microscopy using a two-dimensional spin-polarizing electron mirror *Appl. Phys. Lett.* **99** 032505
- [32] Kaminski D, Poodt P, Aret E, Radenovic N and Vlieg E 2005 Surface alloys, overlayer and incommensurate structures of Bi on Cu(111) *Surf. Sci.* **575** 233–46

- [33] Ünal A A, Tusche C, Ouazi S, Wedekind S, Chiang C-T, Winkelmann A, Sander D, Henk J and Kirschner J 2011 Hybridization between the unoccupied Shockley surface state and bulk electronic states on Cu(111) *Phys. Rev. B* **84** 073107
- [34] Reinert F, Nicolay G, Schmidt S, Ehm D and Hüfner S 2001 Direct measurements of the L-gap surface states on the (111) face of noble metals by photoelectron spectroscopy *Phys. Rev. B* **63** 115415
- [35] Mirhosseini H, Henk J, Ernst A, Ostanin S, Chiang C-T, Yu P, Winkelmann A and Kirschner J 2009 Unconventional spin topology in surface alloys with Rashba-type spin splitting *Phys. Rev. B* **79** 245428
- [36] Bentmann H, Forster F, Bihlmayer G, Chulkov E V, Moreschini L, Grioni M and Reinert F 2009 Origin and manipulation of the Rashba splitting in surface alloys *Europhys. Lett.* **87** 37003
- [37] Matsui F, Miyata H, Rader O, Hamada Y, Nakamura Y, Nakanishi K, Ogawa K, Namba H and Daimon H 2005 Atomic-orbital analysis of the Cu Fermi surface by two-dimensional photoelectron spectroscopy *Phys. Rev. B* **72** 195417